

C-DiffSET: Leveraging Latent Diffusion for SAR-to-EO Image Translation with Confidence-Guided Reliable Object Generation

Jeonghyeok Do

KAIST

ehwjdgur0913@kaist.ac.kr

Jaehyup Lee [†]

KNU

jaehyuplee@knu.ac.kr

Munchurl Kim [†]

KAIST

mkimee@kaist.ac.kr

https://kaist-viclab.github.io/C-DiffSET_site



Figure 1. Qualitative results of SAR-to-EO image translation using our proposed C-DiffSET framework (Confidence Diffusion for SAR-to-EO Translation). Rows 1, 2, and 3 display translations on the QXS-SAROPT, SAR2Opt, and SpaceNet6 datasets, respectively. Our proposed C-DiffSET achieve superior structural accuracy and visual fidelity compared to very recent methods.

Abstract

Synthetic Aperture Radar (SAR) imagery provides robust environmental and temporal coverage (e.g., during clouds, seasons, day-night cycles), yet its noise and unique structural patterns pose interpretation challenges, especially for non-experts. SAR-to-EO (Electro-Optical) image translation (SET) has emerged to make SAR images more perceptually interpretable. However, traditional approaches trained from scratch on limited SAR-EO datasets are prone to overfitting. To address these challenges, we introduce Confidence Diffusion for SAR-to-EO Translation, called C-

DiffSET, a framework leveraging pretrained Latent Diffusion Model (LDM) extensively trained on natural images, thus enabling effective adaptation to the EO domain. Remarkably, we find that the pretrained VAE encoder aligns SAR and EO images in the same latent space, even with varying noise levels in SAR inputs. To further improve pixel-wise fidelity for SET, we propose a confidence-guided diffusion (C-Diff) loss that mitigates artifacts from temporal discrepancies, such as appearing or disappearing objects, thereby enhancing structural accuracy. C-DiffSET achieves state-of-the-art (SOTA) results on multiple datasets, significantly outperforming the very recent image-to-image translation methods and SET methods with large margins.

[†]Co-corresponding authors (equal advising).

1. Introduction

Satellite imagery plays a critical role in various applications, including surveillance, transportation, agriculture, disaster assessment, and environmental monitoring [4, 60, 67, 70, 81]. A significant portion of these applications relies on Electro-Optical (EO) imagery, which provides multi-spectral data captured by EO sensors. However, a fundamental limitation of EO imagery is its susceptibility to weather and lighting conditions, reducing its usability in scenarios such as cloudy weather or nighttime. In contrast, Synthetic Aperture Radar (SAR) offers robust sensing capabilities under all weather conditions without the need for light, making it ideal for nighttime operations. Despite these advantages, SAR imagery presents several challenges. SAR data suffers from speckle noise due to the backscattering of electromagnetic waves [8, 13, 57, 79]. Additionally, SAR images are typically grayscale, lacking the rich spectral and color information in EO images, making them difficult to be interpreted, especially for non-experts. To enhance the usability of SAR data, SAR-to-EO image translation (SET) has emerged as a promising research area in remote sensing, facilitating scene interpretation for tasks such as cloud removal [12, 41, 52] and change detection [38–40].

Recent advancements [14, 25, 28, 31, 32, 50, 54, 75] have demonstrated the potential of generating EO-like outputs from SAR images, offering improved textures and enhanced color information. However, several challenges persist: (i) The domain gap between SAR and EO images makes SET an ill-posed problem, exacerbated by the inherent noise in SAR images; (ii) The misalignment between SAR and EO datasets is prone to occur due to their different sensor platforms, satellite positioning shifts, or acquisition conditions, as shown in Fig. 2; (iii) Temporal misalignments (discrepancies) occur due to different acquisition times, also resulting in the spatial misalignment with differences in object appearance and seasons. This makes it very complicated the SET problem (Fig. 2); (iv) Finally, the scarcity of paired SAR-EO datasets makes it challenging for existing methods to learn the SET effectively, often leading to overfitting or unstable results.

To address these limitations, we *firstly* propose a novel framework that leverages a *pretrained* Latent Diffusion Model (LDM) [11, 47] to improve SAR-to-EO image translation, which is denoted as Confidence Diffusion for SAR-to-EO Translation (C-DiffSET). The advantages of utilizing the pretrained LDM for SET tasks are as follows: (i) Since EO images share visual characteristics with natural images, we fine-tune the pretrained LDM—trained on large-scale natural image datasets—to transfer its representation power to the SET task. This addresses the issue of limited SAR-EO paired data, as our framework can leverage the pretrained knowledge from natural image distributions; (ii) The pretrained LDM operates in a down-sampled latent space

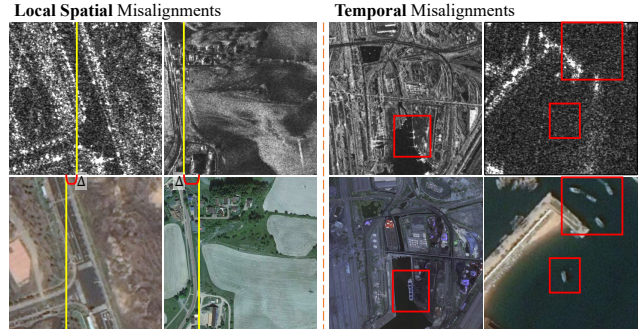


Figure 2. Examples of misalignments in paired SAR-EO datasets. *Left*: Local spatial misalignments caused by sensor differences or acquisition conditions. *Right*: Temporal misalignments (discrepancies) where objects (e.g., ships) appear or disappear between SAR and EO images due to their different acquisition times.

rather than the pixel domain, making it more robust to local spatial misalignments caused by imperfect alignment processes; (iii) The variational auto-encoder (VAE) [29] from LDM can also be applicable for SAR images. As shown in Fig. 4, despite the presence of significant speckle noise in SAR data, the VAE encoder effectively embeds SAR images into the same latent space as EO images, leveraging its denoising capability. This enables the smooth transfer of SAR latents as conditioning information in the reverse diffusion process, ensuring the generation of EO outputs with accurate pixel-wise correspondence to the SAR inputs.

In addition to utilizing the pretrained LDM as a foundation model for our SET task, we introduce a confidence-guided diffusion (C-Diff) loss to handle temporal discrepancies. The temporal discrepancies, such as objects appearing in only one modality, can introduce artifacts and hallucinated content in the generated EO images. To mitigate this, the U-Net [48] in our framework predicts both each predicted noise and its corresponding confidence map, which quantifies the pixel-wise uncertainty in the predicted noise. The U-Net receives a channel-wise concatenated SAR and noisy EO features as input, allowing it to jointly model both contexts. This setup enables the confidence map to reflect the inherent uncertainty caused by temporal discrepancies, guiding the C-Diff loss to adaptively reduce penalties in regions where SAR-EO misalignments likely occur. As a result, the generated EO images achieve high pixel-wise fidelity while minimizing artifacts and hallucinations. Our key contributions are summarized as:

- We propose C-DiffSET, the *first* framework to fine-tune a *pretrained* LDM for SET tasks, effectively leveraging their learned representations to overcome the scarcity of SAR-EO pairs and local misalignment challenges.
- We introduce a novel C-Diff loss that can guide our C-DiffSET to reliably predict both EO outputs and confidence maps for accurate SET.

- We validate our C-DiffSET through extensive experiments on datasets with varying resolutions and ground sample distances (GSD) [61], including QXS-SAROPT [19], SAR2Opt [80], and SpaceNet6 [56] datasets, demonstrating the superiority of our C-DiffSET that *significantly* outperforms the very recent image-to-image translation methods and SET methods with large margins.

2. Related Work

2.1. Image-to-Image Translation

Image-to-image translation has been widely studied in various fields, such as image colorization [76, 77], style transfer [24, 55, 84], and image inpainting [22, 43]. These models typically rely on carefully constructed paired datasets across domains for effective training. For instance, Pix2Pix [24] introduced conditional GANs with an l_1 loss for domain-specific translations, while ASAPNet [55] proposed a lightweight framework for converting segmentation maps into realistic images, demonstrating abstract-to-detailed generation. However, acquiring paired datasets remains challenging, and various methods have been proposed to work around unpaired data constraints [1, 27, 35]. CycleGAN [84] addressed this limitation using a cycle-consistency loss to facilitate training without paired data. StarGAN [7] extended this idea to support multiple domain mappings within a single model, though its deterministic one-to-one approach limits flexibility. MUNIT [20] overcame this by decomposing images into domain-invariant content and domain-specific style representations, enabling diverse mappings while maintaining content integrity. Further addressing non-bijective translation, StegoGAN [69] introduced steganography into GAN-based models, enhancing semantic consistency in cases of domain mismatch by reducing spurious features in generated images without additional supervision.

Diffusion-based approaches. Diffusion models [11, 17, 18, 33, 44, 47, 49], have gained significant attraction in image-to-image translation due to their iterative denoising process, effectively modeling complex data distributions. Palette [49] utilizes conditional Denoising Diffusion Probabilistic Models (DDPMs) [18] in the pixel domain, achieving high-quality translations. Pixel-space operations often incur high computational costs for high-resolution images, motivating recent advances that utilize latent space diffusion to achieve greater efficiency. BBDM [33] diffuses directly from input to target latent space, eliminating the need for separate noise conditioning but imposing strict pixel-wise alignment requirements between input and target images. DGDM [71] is built on BBDM with a deterministic approach, where a translator network generates target features prior to diffusion, adding computational overhead and dependency on the initial translator’s performance.

2.2. SAR-to-EO Image Translation (SET)

Deep learning-based image-to-image translation methods [1, 20, 22, 24, 33, 35, 55, 82] have been widely adopted to remote sensing applications, including SAR-to-EO image translation (SET). However, SAR imagery poses unique challenges due to inherent characteristics like speckle noise from backscattering effects [8, 13, 21, 57, 59, 74, 79], complicating the translation process. To address these challenges, most SET studies employ GAN-based approaches [5, 9, 30, 32, 63, 66, 72, 75]. Conditional GAN-based models are commonly used to leverage noisy SAR information as a conditioning input, while CycleGAN-based models align the SAR and EO domains by enforcing cycle-consistency constraints. MCGAN [25] utilized a CycleGAN-based model, incorporating a mask vector with class labels to represent different regions. DTCDN [34] employed NICE-GAN [6] for joint SET and change detection tasks, improving feature alignment between domains. PLFM [52] introduced a multimodal model that integrates spatial and temporal data with SAR guidance images to produce clear EO outputs. Additionally, CFCA-SET [31] proposed a coarse-to-fine SAR-to-EO model that incorporates near-infrared (NIR) images during training to refine EO generation.

Diffusion-based approaches. Recently, a limited number of diffusion-based studies have been explored for SET, primarily divided into DDPM-based [2, 3] and LDM-based [14, 28, 54] methods. DSE [54] utilize the BBDM [33] to generate EO predictions for downstream tasks like flood segmentation. Expanding on this, cBBDM [28] integrates SAR inputs as conditional information in BBDM to improve translation quality, while CM-Diffusion [14] further enhances BBDM by conditioning on color features, helping to preserve spectral consistency in EO generation.

Despite these advancements, both GAN-based and diffusion-based methods encounter limitations stemming from the scarcity of paired SAR-EO datasets. GAN-based models frequently face with convergence challenges and mode collapse under limited data, while diffusion-based approaches struggle with overfitting and slow convergence due to the need for extensive training from scratch. To overcome these constraints, our C-DiffSET leverages a pre-trained LDM as foundational model. By capitalizing on the extensive generative priors of large-scale text-to-image models, the C-DiffSET effectively adapts to the SET task, achieving robust translation with a reduced overfitting risk.

2.3. Latent Diffusion Models (LDMs)

Latent Diffusion Models (LDMs) [11, 47] extend the foundational DDPMs [18], which apply iterative noise addition to pixel-space images in a forward process, transforming them toward following Gaussian distribution. DDPMs are trained to reverse this process, step-by-step denoising to

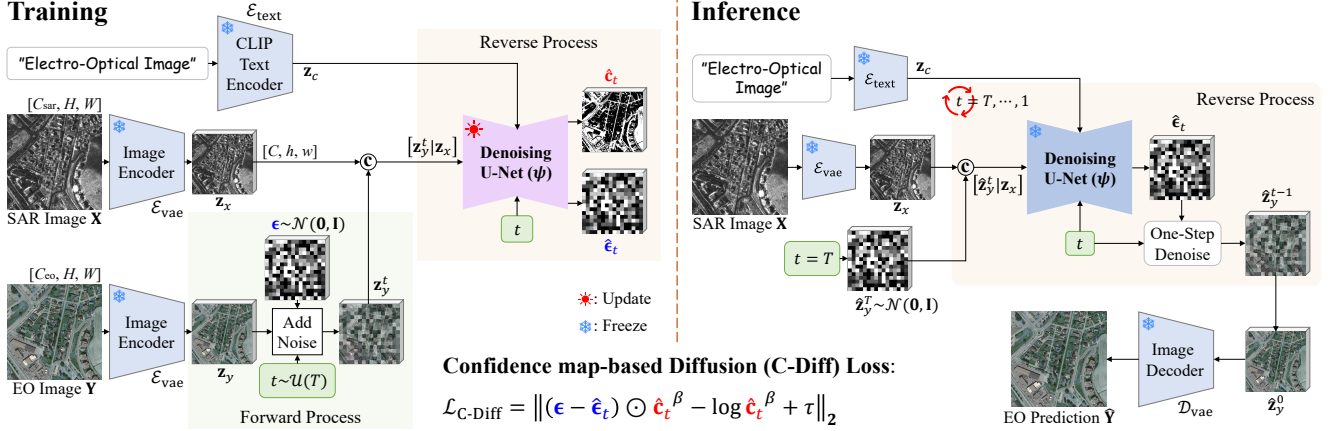


Figure 3. Overall framework of our Confidence Diffusion for SAR-to-EO Translation (C-DiffSET).

recover high-quality images. While effective for complex data modeling, DDPMs are computationally demanding in high-resolution applications due to their pixel-space processing. In contrast, LDMs address this by shifting the diffusion process to a learned latent space, significantly reducing memory requirements and computational costs. Using a VAE to encode images into a compact latent space, LDMs perform denoising directly on these representations, retaining high-resolution details with improved efficiency.

LDMs as foundation models. Open-source [62] releases of foundation LDMs, such as Stable Diffusion (v1.5, v2.1, v3.0) [11, 47], SDXL [45], both of which were pretrained on extensive text-to-image (T2I) datasets (i.e., LAION-5B [51]), have fueled progress across generative domains. These models offer powerful priors for image synthesis, and have been widely adapted through fine-tuning, particularly for natural image applications [15, 26, 68, 73]. Leveraging their strong generative capacity, we adapt a pretrained LDM for the SET task.

3. Methods

3.1. Overview of Proposed C-DiffSET

We utilize a paired SAR-EO dataset $\mathcal{I} = \{(\mathbf{X}, \mathbf{Y})\}$, where $\mathbf{X} \in \mathbb{R}^{C_{\text{sar}} \times H \times W}$ represents SAR images of $H \times W$ sizes and C_{sar} channels and $\mathbf{Y} \in \mathbb{R}^{C_{\text{eo}} \times H \times W}$ denotes EO images of $H \times W$ sizes and C_{eo} channels. Our goal is to generate a predicted EO image $\hat{\mathbf{Y}}$ corresponding to the given SAR input \mathbf{X} . Fig. 3 illustrates the proposed Confidence Diffusion for SAR-to-EO Translation (C-DiffSET) framework, which comprises three key components: (i) the embedding of SAR and EO images into the latent space, (ii) the forward diffusion process, and (iii) the reverse diffusion process with the confidence-guided diffusion (C-Diff) loss. As described in Sec. 3.2, SAR image \mathbf{X} and EO image \mathbf{Y} are passed through the VAE encoder \mathcal{E}_{vae} , generating the latent

features $\mathbf{z}_x \in \mathbb{R}^{C \times h \times w}$ (SAR feature) and $\mathbf{z}_y \in \mathbb{R}^{C \times h \times w}$ (EO feature). In the forward diffusion process (Sec. 3.3), noise ϵ is added to the EO feature \mathbf{z}_y over timesteps t s. During the reverse diffusion process, the U-Net ψ takes the noisy EO feature \mathbf{z}_y^t , the timestep t , and the SAR feature \mathbf{z}_x as conditional inputs. The Denoising U-Net ψ predicts both the noise $\hat{\epsilon}_t$ and a confidence map \hat{c}_t that quantifies pixel-wise uncertainty of the prediction. Finally, in Sec. 3.4, we describe the inference stage, where the predicted EO image $\hat{\mathbf{Y}}$ is generated by reversing the noise-added process.

3.2. SAR and EO Latent Space Generation

We utilize the pretrained VAE from LDM for mapping input images from the pixel space to the latent space. The VAE is frozen during our experiments and serves as both an encoder \mathcal{E}_{vae} and a decoder \mathcal{D}_{vae} for input images. Since the LDM has been pretrained on large-scale natural image datasets, the VAE is designed to accept 3-channel RGB images as input. Fig. 4 shows the results of applying the VAE encoder \mathcal{E}_{vae} and decoder \mathcal{D}_{vae} to SAR and EO images, validating its applicability for both modalities.

EO latent space. Since EO images \mathbf{Y} are naturally represented as 3-channel RGB inputs, they are directly passed through the VAE without modification. In our experiments, we confirmed that the reconstruction error $\|\mathbf{Y} - \mathcal{D}_{\text{vae}}(\mathcal{E}_{\text{vae}}(\mathbf{Y}))\|_2$ is minimal, ensuring that the VAE accurately preserves the content and structure of EO images. This indicates that the VAE’s output provides an upper bound on the achievable performance of our framework, serving as a stable baseline for EO image generation.

SAR latent space. SAR data \mathbf{X} , depending on the satellite sensors, is available as single-polarization SAR images of 1-channel (HH or VV component) or full-polarization ones of 4-channel (HH, HV, VH, and VV components). For 1-channel SAR images, we repeat the channel three times to match the VAE’s input requirements. For 4-channel SAR

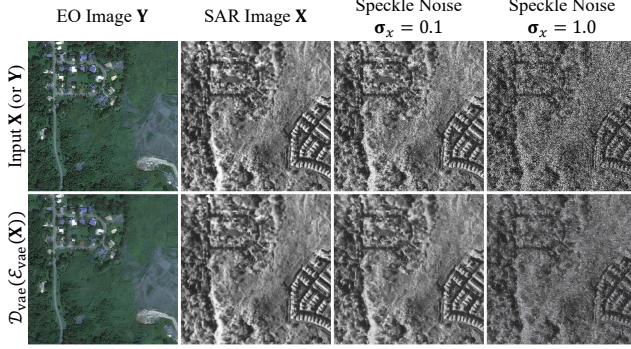


Figure 4. Results of applying the VAE encoder and decoder from LDM to EO and SAR images. The first row shows input images, including EO and SAR images with different levels of speckle noise. The second row presents the corresponding VAE reconstructions, illustrating that both EO and SAR images are accurately reconstructed despite noise variations.

data, we construct a 3-channel input by using HH, the average of HV and VH, and VV components. After passing these inputs through the VAE, we observed that the reconstruction error $\|\mathbf{X} - \mathcal{D}_{\text{vae}}(\mathcal{E}_{\text{vae}}(\mathbf{X}))\|_2$ remained low, and the outputs appeared visually pleasing, as shown in Fig. 4. Additionally, we examined the VAE’s behavior under varying levels of speckle noise added to SAR inputs. The results demonstrate that the VAE’s reconstruction process adapts spatially to the noise level, effectively denoising the inputs while preserving structural details. This suggests that the VAE can embed SAR images into the same latent space as EO images without additional training, allowing SAR features to serve as conditioning inputs during the diffusion process. This ensures that pixel-wise correspondence between SAR and EO latent spaces is maintained throughout the generation process.

3.3. Training Strategy for the Diffusion Process

The diffusion process consists of two key stages: a forward process that progressively adds noise to the target EO feature, and a reverse process that Denoising U-Net ψ predicts and removes the added noise.

Forward process. Following the DDPMs [18] framework, noise is added to the target EO feature \mathbf{z}_y over a sequence of timesteps $t \sim \mathcal{U}(T)$, where \mathcal{U} is a uniform distribution and T is a total number of timesteps. Specifically, at each timestep t , a noisy version of the EO feature \mathbf{z}_y^t is generated by sampling:

$$\mathbf{z}_y^t = \sqrt{\bar{\alpha}_t} \mathbf{z}_y + \sqrt{1 - \bar{\alpha}_t} \boldsymbol{\epsilon}, \quad \boldsymbol{\epsilon} \sim \mathcal{N}(\mathbf{0}, \mathbf{I}), \quad (1)$$

where \mathcal{N} is a Gaussian distribution, $\boldsymbol{\epsilon} \in \mathbb{R}^{C \times h \times w}$, and $\bar{\alpha}_t = \prod_{s=1}^t (1 - \beta_s)$ [18] determines the noise magnitude at each timestep t .

Reverse process. ψ learns the reverse process by predicting the added noise $\boldsymbol{\epsilon}$, aligning with the pretrained LDM design. To leverage the pre-trained LDM’s text-to-image capability and provide a strong initialization, we use a fixed prompt, $p = \text{“electro-optical image”}$, as a stable conditioning signal. This guides the LDM to focus on EO-specific features by embedding the prompt via the CLIP [46] text encoder $\mathcal{E}_{\text{text}}$ as $\mathbf{z}_c = \mathcal{E}_{\text{text}}(p)$, rather than using a null prompt. ψ takes as input the noisy EO feature \mathbf{z}_y^t and conditioned SAR feature \mathbf{z}_x , concatenated along the channel dimension, and is also fed with the timestep t and the text prompt embedding \mathbf{z}_c . Then, we have two output components: a predicted noise $\hat{\boldsymbol{\epsilon}}_t$ and a confidence map $\hat{\mathbf{c}}_t \in \mathbb{R}^{1 \times h \times w}$ that contains the pixel-wise uncertainty of $\hat{\boldsymbol{\epsilon}}_t$:

$$[\hat{\boldsymbol{\epsilon}}_t | \hat{\mathbf{c}}_t] = \psi([\mathbf{z}_y^t | \mathbf{z}_x], \mathbf{z}_c, t), \quad (2)$$

where $[\cdot | \cdot]$ indicates channel-wise concatenation. The confidence map $\hat{\mathbf{c}}_t$ is further processed through a SoftPlus [10] operation to ensure all values remain non-negative.

Confidence-guided diffusion (C-Diff) loss. Seitzer *et al.* [53] proposed the β -NLL loss to capture aleatoric uncertainty for regression, classification and generative tasks. Inspired by the β -NLL loss [53, 64], we firstly adopt it into the training stage of diffusion process to enhance pixel-wise fidelity and to manage temporal inconsistencies between SAR and EO images. We apply the confidence output of ψ at each diffusion step to the β -NLL loss for stable SET, which is called C-Diff loss $\mathcal{L}_{\text{C-Diff}}$. That is, $\mathcal{L}_{\text{C-Diff}}$ uses a learned confidence map $\hat{\mathbf{c}}_t$ to adaptively weight the predicted noise $\hat{\boldsymbol{\epsilon}}_t$ pixel-wise. $\mathcal{L}_{\text{C-Diff}}$ is designed to prioritize high-confidence areas while downweighting uncertain regions, thus improving robustness in regions with temporal misalignments (e.g., dynamic objects in SAR or EO images). $\mathcal{L}_{\text{C-Diff}}$ optimizes ψ by combining a weighted pixel-wise reconstruction loss and a regularization term for the confidence map $\hat{\mathbf{c}}_t$:

$$\mathcal{L}_{\text{C-Diff}} = \left\| (\boldsymbol{\epsilon} - \hat{\boldsymbol{\epsilon}}_t) \odot \hat{\mathbf{c}}_t^\beta - \log \hat{\mathbf{c}}_t^\beta + \tau \right\|_2, \quad (3)$$

where τ is a margin term ensuring non-negativity of the loss, and $\beta = 1$. $\hat{\mathbf{c}}_t$ effectively acts as an adaptive weighting factor, allowing the model to focus more on well-aligned regions and reduce penalties in uncertain areas. The log term serves as a regularizer, preventing $\hat{\mathbf{c}}_t$ from collapsing to zero. $\mathcal{L}_{\text{C-Diff}}$ allows C-DiffSET to produce EO outputs of high structural accuracy while mitigating artifacts and hallucinations that can arise in temporally inconsistent regions.

3.4. Inference Stage for EO Image Prediction

Given an unseen SAR image \mathbf{X} , we pass it through the VAE encoder \mathcal{E}_{vae} to obtain its SAR latent code $\mathbf{z}_x = \mathcal{E}_{\text{vae}}(\mathbf{X})$, which serves as the conditioning information for the reverse diffusion process. For inference, the Denoising U-Net ψ

iteratively refines the noisy latent code $\hat{\mathbf{z}}_y^T$, to reconstruct the target EO latent code $\mathbf{z}_y^0 = \mathbf{z}_y$ by denoising it back to the clean EO latent code through noise prediction $\hat{\epsilon}_t$. Starting from pure noise, $\hat{\mathbf{z}}_y^T \sim \mathcal{N}(\mathbf{0}, \mathbf{I})$, ψ iteratively refines the EO latent code $\hat{\mathbf{z}}_y^t$ by predicting the noise $\hat{\epsilon}_t$ to be removed at each timestep t as:

$$[\hat{\epsilon}_t \mid \text{Dummy}] = \psi([\hat{\mathbf{z}}_y^t \mid \mathbf{z}_x], \mathbf{z}_c, t), \quad (4)$$

where Dummy indicates dummy confidence values. The predicted noise $\hat{\epsilon}_t$ is then used to compute $\hat{\mathbf{z}}_y^{t-1}$ in the reverse diffusion process, following the formulation in [18], which progressively denoises the EO latent code until it converges to the target EO latent code. The final EO latent code $\hat{\mathbf{z}}_y^0$ is passed through the VAE decoder \mathcal{D}_{vae} to generate the reconstructed EO image $\hat{\mathbf{Y}} = \mathcal{D}_{\text{vae}}(\hat{\mathbf{z}}_y^0)$.

4. Experiment

4.1. Datasets

We evaluate our C-DiffSET framework on three publicly available SAR-to-EO datasets: QXS-SAROPT [19], SAR2Opt [80], and SpaceNet6 [56]. These datasets vary in satellite platforms, GSD [61], and SAR polarization modes, allowing us to assess the robustness and generalizability of our approach across diverse real-world scenarios.

QXS-SAROPT [19]. The QXS-SAROPT dataset contains 20,000 SAR and EO image pairs captured by the Gaofen-3 satellite (SAR) and Google Earth (EO). The SAR images are acquired in a single-polarization mode. The EO images consist of RGB channels, covering various port cities. Each image patch measures 256×256 pixels with an 1-m GSD, focusing on complex maritime environments.

SAR2Opt [80]. The SAR2Opt dataset provides 2,076 SAR and EO image pairs obtained from the TerraSAR-X satellite (SAR) and Google Earth (EO). The SAR images are captured in a single-polarization mode. The corresponding EO images contain RGB channels and cover diverse Asian cities. Each patch measures 600×600 pixels with an 1-m GSD, making this dataset particularly useful for urban area analysis and infrastructure monitoring.

SpaceNet6 [56]. The SpaceNet6 dataset offers SAR and EO image pairs captured by Capella Space (SAR) and Maxar WorldView-2 (EO) satellites. The SAR images are acquired with full-polarization, enabling detailed analysis of surface structures. The EO images include RGB and NIR bands, though only the RGB subset is used in our experiments. This dataset contains 3,401 SAR-EO image pairs, with each patch size of 900×900 pixels and a 0.5-m GSD, focusing on urban landscapes and building detection tasks.

4.2. Experiment Details

All experiments were implemented using PyTorch [42] and conducted on a single NVIDIA A6000 GPU. Each

model was fine-tuned for 50,000 iterations, with a 100-step warmup period. We employed the AdamW optimizer [36] with an initial learning rate of 3×10^{-5} and a weight decay of 0.01. A cosine-annealing scheduler [37] was used to progressively reduce the learning rate at each iteration. For the pretrained LDM, we utilized Stable Diffusion v2.1 [47, 62], and the text encoder was frozen as the CLIP-ViT-H/14 [23, 46] text encoder. For the latent features, we set the spatial resolution parameters as $h = H/8$, $w = W/8$, and the channel dimension as $C = 4$. The training noise scheduler was based on DDPM [18] with a total of 1,000 steps. For inference, we employed a more efficient DDIM [58] noise scheduler with total 50 inference steps to accelerate the generation process. Since SAR features were incorporated as additional inputs to the U-Net ψ , the weights of the ψ 's first convolutional layer were initialized by repeating the original weights across the SAR channels. Additionally, the confidence map was initialized to 1 to ensure stable optimization, starting from the standard ℓ_2 loss, and $\tau = \log 2\pi$ [53] was applied. For the QXS-SAROPT dataset, we used the provided original 256×256 -sized patches without modification, with a batch size of 64. For the SAR2Opt and SpaceNet6 datasets, we performed random cropping to 512×512 -sized patches and set the batch size to 16. Data augmentation techniques, including random horizontal and vertical flips and random rotations (multiples of 90 degrees), were applied during training to improve generalization. To ensure reproducibility, a random seed of 2,025 was fixed for all experiments. Data was split with 80% used for training and 20% for testing across all experiments. We evaluated the performance of our framework using Fréchet Inception Distance (FID) [16], Learned Perceptual Image Patch Similarity (LPIPS) [78], Spatial Correlation Coefficient (SCC) [83], Structural Similarity Index (SSIM) [65], and Peak Signal-to-Noise Ratio (PSNR).

4.3. Experimental Results

For comparative analysis, we used official implementations for general image-to-image translation methods [24, 33, 69, 71, 84]. For SET-specific methods [28, 31] (marked by †), where official codes are generally unavailable due to the specialized nature of the field, we re-implemented each method according to their technical descriptions.

Qualitative comparison. As illustrated in Fig. 1, Fig. 5, and Fig. 6, the GAN-based methods generally struggle with stability during training, leading to prominent artifacts in SET. The LDM-based methods, such as BBDM [33] and cBBDM [28], face challenges due to their reliance on direct diffusion from SAR input \mathbf{X} to EO output \mathbf{Y} . This setup makes them particularly susceptible to local spatial misalignments, producing blurred and incoherent results. DGDM [71] seeks to improve the initial stage of diffusion through a deterministic approach, employing a lightweight

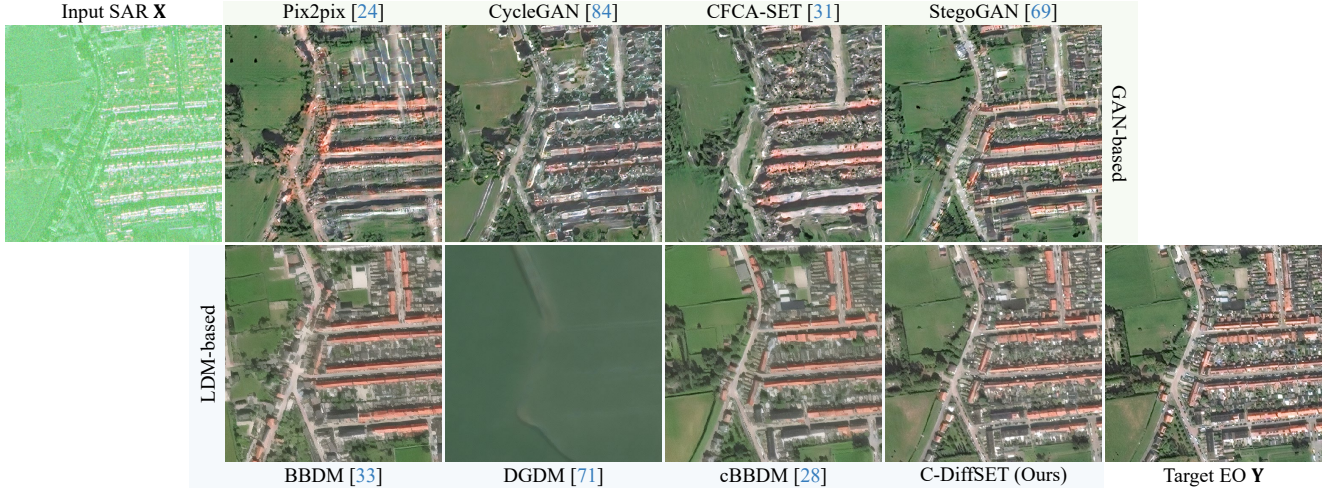


Figure 5. Qualitative SAR-to-EO image translation on the SpaceNet6 dataset. Top row: GAN-based methods (Pix2pix, CycleGAN, CFCA-SET, and StegoGAN). Bottom row: LDM-based methods (BBDM, DGDM, cBBDM, and C-DiffSET).

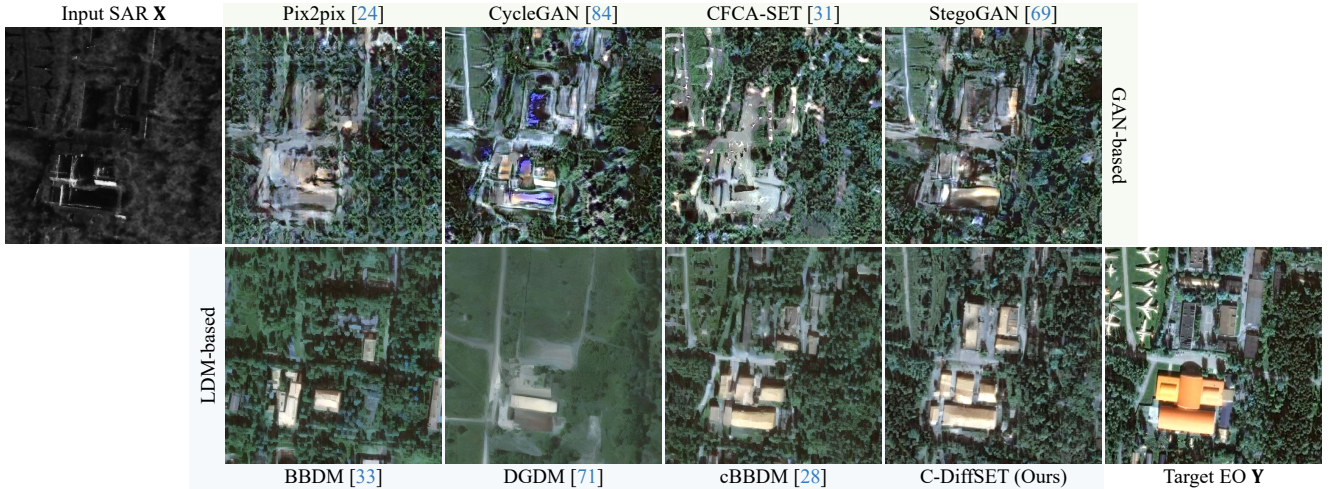


Figure 6. Qualitative SAR-to-EO image translation results on the SAR2Opt dataset. Top row: GAN-based methods (Pix2pix, CycleGAN, CFCA-SET, and StegoGAN). Bottom row: LDM-based methods (BBDM, DGDM, cBBDM, and C-DiffSET).

translation network to create a translated EO latent from SAR latent. However, the simplistic nature of this translation network fails to capture the intricate EO features, resulting in suboptimal initial latents for the diffusion process. In contrast, our C-DiffSET leverages pretrained LDM as foundational model, effectively addressing alignment issues via a confidence-guided diffusion loss, leading to yield sharper and more structurally coherent EO images, and to outperform both GAN-based and diffusion-based baselines in visual fidelity. Notably, as shown in Fig. 6, slight discrepancies between our generated EO images and the target EO images can occur. These differences arise from our model’s emphasis on structural alignment with the input SAR image, prioritizing SAR-EO correspondence over exact visual matching with the target EO.

Quantitative evaluation. In the quantitative assessment (see Table 1 and Table 2), the GAN-based methods yield lower PSNR, SSIM, and SCC scores, indicating their propensity for artifacts and limited spatial coherence. The LDM-based methods, BBDM and cBBDM, also perform inadequately due to their direct diffusion setup from SAR to EO, which exacerbates pixel-wise misalignment issues and inflates LPIPS and FID scores. The DGDM incorporates a lightweight translator network to initialize the diffusion process, but its simplistic structure fails to encapsulate detailed EO features, resulting in lower PSNR and SSIM scores. In contrast, our C-DiffSET achieves superior performance across all metrics, enabled by pretrained LDM and the confidence-guided diffusion loss, which jointly tackles SAR-specific noise and alignment challenges. This adap-

Types	Methods	Publications	SAR2Opt Dataset					SpaceNet6 Dataset				
			FID↓	LPIPS↓	SCC↑	SSIM↑	PSNR↑	FID↓	LPIPS↓	SCC↑	SSIM↑	PSNR↑
GANs	Pix2Pix [24]	CVPR 2017	196.87	0.426	0.0006	0.216	15.422	124.55	0.256	0.0102	0.522	19.357
	CycleGAN [84]	ICCV 2017	139.72	0.425	0.0022	0.224	14.931	114.81	0.274	0.0097	0.493	17.798
	CFCA-SET [†] [31]	TGRS 2023	152.27	0.430	0.0009	0.223	15.183	164.78	0.279	0.0097	0.498	18.297
	StegoGAN [69]	CVPR 2024	144.54	0.398	0.0034	0.237	15.624	75.12	0.244	0.0106	0.516	18.958
LDMs	BBDM [33]	CVPR 2023	94.72	0.473	0.0005	0.234	15.131	81.86	0.302	0.0019	0.217	17.678
	DGDM [71]	ECCV 2024	156.12	0.541	0.0004	0.273	15.568	238.37	0.438	0.0015	0.253	17.124
	cBBDM [†] [28]	arXiv 2024	97.64	0.394	0.0022	0.285	16.591	72.77	0.243	0.0079	0.254	19.033
	C-DiffSET (Ours)	-	77.81	0.346	0.0035	0.286	16.613	37.44	0.142	0.0151	0.567	21.022

Table 1. Quantitative comparison of image-to-image translation methods and SET methods on SAR2Opt and SpaceNet6 datasets. **Red** indicate the best performance in each metric.

Types	Methods	QXS-SAROPT Dataset				
		FID↓	LPIPS↓	SCC↑	SSIM↑	PSNR↑
GANs	Pix2Pix [24]	196.89	0.454	0.0000	0.247	14.924
	CycleGAN [84]	195.38	0.455	0.0001	0.251	14.977
	CFCA-SET [†] [31]	79.06	0.406	0.0006	0.273	15.094
	StegoGAN [69]	85.60	0.391	0.0019	0.280	15.580
LDMs	BBDM [33]	65.15	0.522	0.0004	0.238	13.946
	DGDM [71]	147.23	0.634	0.0001	0.288	11.564
	cBBDM [†] [28]	69.47	0.420	0.0023	0.304	16.248
	C-DiffSET (Ours)	18.15	0.293	0.0108	0.372	18.077

Table 2. Quantitative comparison of image-to-image translation methods and SET methods on the QXS-SAROPT dataset. **Red** values represent the best results.

Pretrained LDM	\mathcal{L}_{C-Diff}	SAR2Opt Dataset				
		FID↓	LPIPS↓	SCC↑	SSIM↑	PSNR↑
		98.98	0.385	0.0014	0.255	15.815
✓		78.14	0.349	0.0029	0.280	16.460
✓	✓	77.81	0.346	0.0035	0.286	16.613

Table 3. Ablation study on the SAR2Opt dataset evaluating the impact of pretrained LDM and confidence-guided diffusion loss.

tation allows the C-DiffSET to attain the highest PSNR, SSIM, and SCC values, along with the lowest LPIPS and FID scores, highlighting its enhanced fidelity and perceptual quality in SET.

4.4. Ablation Studies

Impact of pretrained LDM and \mathcal{L}_{C-Diff} . To assess the contribution of the pretrained LDM and the confidence-guided diffusion loss \mathcal{L}_{C-Diff} , we conducted an ablation study on the SAR2Opt dataset, as shown in Table 3. The pretrained LDM provides strong initialization for EO generation, improving the baseline PSNR and SSIM scores when compared to training from scratch. Furthermore, incorporating \mathcal{L}_{C-Diff} somewhat enhances these metrics and lowers LPIPS and FID values, improving both perceptual fidelity and structural consistency. Fig. 7 shows confidence maps generated on the training dataset at timestep $t = T/2$ (mid-point of the denoising process), highlighting the areas of temporal discrepancy in SAR-EO pairs. This loss enables the U-Net ψ to down-weight uncertain regions where objects are temporally misaligned across modalities, thereby reducing artifacts and ensuring coherent EO outputs.

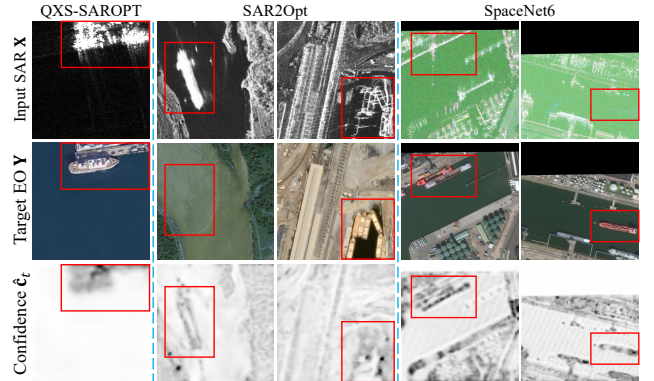


Figure 7. Confidence maps generated by C-DiffSET at timestep $t = T/2$ on SAR-EO paired datasets: QXS-SAROPT, SAR2Opt, and SpaceNet6. Each row illustrates the input SAR image X , the target EO image Y , and the corresponding confidence map \hat{c}_t .

4.5. Limitations

Scalability across diverse satellites. The VAE in C-DiffSET is designed for 3-channel inputs, matching typical RGB images. This limits its direct application to datasets with more channels (e.g., RGB+NIR or multispectral data). An extension to supporting such inputs would require further exploration and tuning for effective adaptation.

5. Conclusion

In this work, we propose C-DiffSET, a novel framework that addresses key challenges in SAR-to-EO image translation. To the best of our knowledge, this is the first method to fully leverage LDM for SET tasks, mitigating issues caused by the limited availability of paired datasets. We introduce a C-Diff loss to handle temporal discrepancy between SAR and EO acquisitions, ensuring pixel-wise fidelity by adaptively suppressing artifacts and hallucinations. C-DiffSET achieves SOTA performance across datasets with varying GSD, demonstrating its effectiveness in real-world scenarios. Our framework provides a scalable foundation for future SET research and can be extended to other remote sensing applications and modalities.

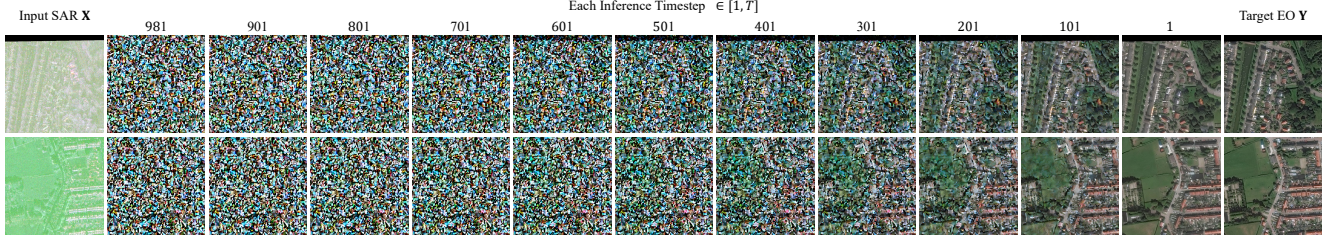


Figure 8. Visualization of C-DiffSET results across inference timesteps on the SpaceNet6 dataset with a total of 50 inference steps. Each column corresponds to an inference step, starting with substantial noise at $t = 981$ and progressively refining the output to match the target EO image at $t = 1$.

A. Additional Discussions on Results

A.1. Additional Qualitative Comparisons

Fig. 11, Fig. 12, Fig. 13, Fig. 14, Fig. 15, Fig. 16, and Fig. 17 provide additional qualitative comparisons of SAR-to-EO image translation results on the QXS-SAROPT [50], SAR2Opt [80], and SpaceNet6 [56] dataset. The GAN-based methods, including Pix2Pix [24] and CycleGAN [84], exhibit severe artifacts due to inherent unstable training in GAN frameworks. Although CFCA-SET [31] and StegoGAN [69] mitigate some of these artifacts, they still produce visually inconsistent results, often failing to preserve fine-grained structural details. Among the LDM-based approaches, BBDM [33] and cBBDM [28] generate smoother outputs and struggle with oversimplified textures and lack of structural alignment due to their direct diffusion process. DGDM [71], on the other hand, relies on an initial translator network to generate SAR-to-EO latents; however, the simplicity of this translator leads to poorly initialized latents, resulting in entirely unrealistic outputs. In contrast, our proposed C-DiffSET effectively addresses these limitations, producing visually coherent and structurally accurate EO images that are closely aligned with the target EO images.

A.2. Progressive Denoising Visualization

Fig. 8 illustrates the progression of generated images across different inference timesteps during the reverse denoising process. Out of the total $T_{\text{test}} = 50$ inference steps, we select 11 representative timesteps to visualize the progressive refinement of the output. Using the DDIM [58] noise scheduler, denoising is performed over 50 steps, with timesteps chosen from the range $[1, T]$ to balance sampling efficiency and performance. At earlier timesteps (e.g., $t = 981$), the images exhibit significant noise, reflecting the initial latent representation. As the process progresses to later timesteps (e.g., $t = 1$), the generated images become increasingly coherent, closely resembling the target EO images.

Methods	First 50 samples from the SpaceNet6 Dataset				
	FID↓	LPIPS↓	SCC↑	SSIM↑	PSNR↑
C-DiffSET (Ours)	85.77	0.132	0.0210	0.546	21.498
$\mathcal{D}_{\text{vae}}(\mathcal{E}_{\text{vae}}(\mathbf{Y}))$	43.57	0.049	0.1631	0.783	28.633

Table 4. Comparison of C-DiffSET performance with the VAE upper bound on the SpaceNet6 dataset. The upper bound represents the maximum achievable quality defined by the VAE-decoded target EO features.

A.3. Analysis of VAE Reconstruction and Upper Bound Performance

In Fig. 4, we evaluate the reconstruction quality of the VAE encoder \mathcal{E}_{vae} and decoder \mathcal{D}_{vae} from the LDM by visualizing their outputs for target EO images and SAR images with varying levels of speckle noise. Our proposed C-DiffSET framework, built upon the LDM architecture, predicts target EO features $\mathbf{z}_y = \mathcal{E}_{\text{vae}}(\mathbf{Y})$ embedded in the latent space through the VAE encoder. Thus, the VAE-decoded reconstruction of the target EO feature, $\mathcal{D}_{\text{vae}}(\mathcal{E}_{\text{vae}}(\mathbf{Y}))$, serves as an upper bound for our C-DiffSET, representing the maximum achievable quality given the pre-trained LDM. Table 4 quantitatively compares the performance of C-DiffSET with this upper bound. While our framework delivers strong results, especially in terms of perceptual metrics such as LPIPS and FID, the gap to the upper bound highlights the inherent limitations in SAR-to-EO image translation due to noise, misalignments, and the complexities of SAR data. This analysis underscores the potential for future work to narrow this gap, advancing SAR-to-EO image translation toward the limits defined by the upper bound.

B. Further Ablation Studies

B.1. Effect of Total Inference Steps

In Fig. 9 and Fig. 10, we justify the selection of $T_{\text{test}} = 50$ inference steps in our experiments. While setting the total inference steps to match the training steps ($T = 1,000$) ensures high performance, it incurs prohibitive inference

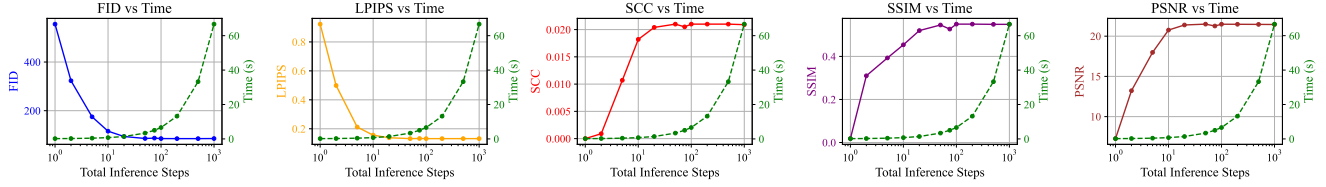


Figure 9. Impact of total inference steps on performance metrics (FID, LPIPS, SCC, SSIM, and PSNR) and inference time.



Figure 10. Visualization of C-DiffSET results across varying numbers of total inference steps.

times. To balance performance and efficiency, we evaluate the tradeoff between inference time and metric performance by varying the DDIM noise scheduler’s inference steps. For computational feasibility, experiments are conducted on the first 50 samples of the SpaceNet6 dataset. The results indicate significant performance gains for lower step counts ($T_{\text{test}} = 1$ to $T_{\text{test}} = 50$), but diminishing returns beyond 50 steps, with negligible improvements in metrics such as FID, LPIPS, and PSNR. Based on this analysis, we select total 50 inference steps as the optimal tradeoff, achieving high-quality outputs within practical inference times (3.376 second per 512×512 image).

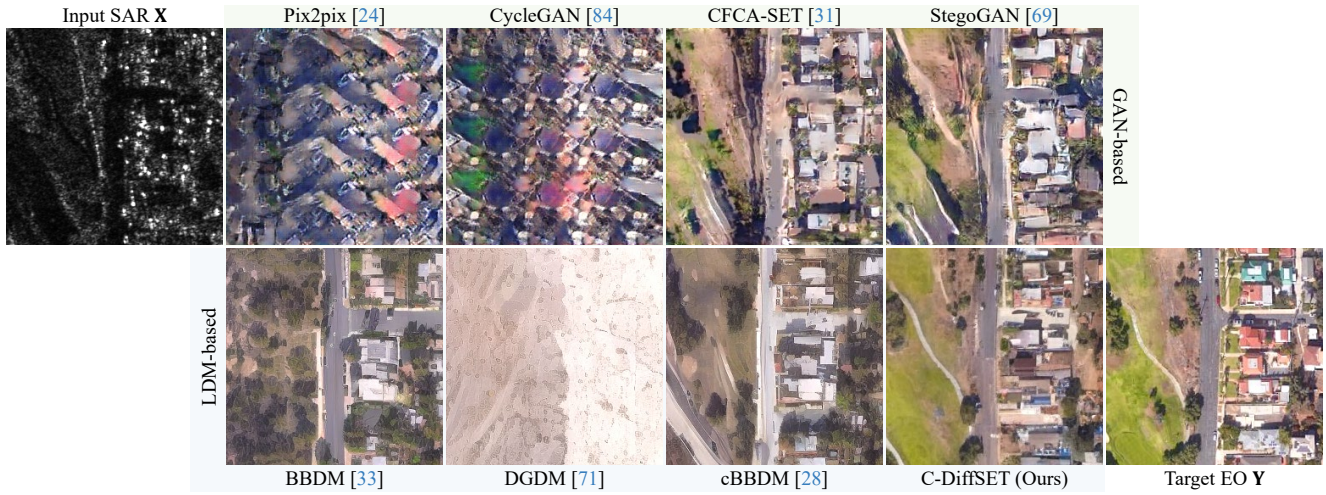


Figure 11. Qualitative SAR-to-EO image translation on the QXS-SAROPT dataset. Top row: GAN-based methods (Pix2pix, CycleGAN, CFCA-SET, and StegoGAN). Bottom row: LDM-based methods (BBDM, DGDM, cBBDM, and C-DiffSET).

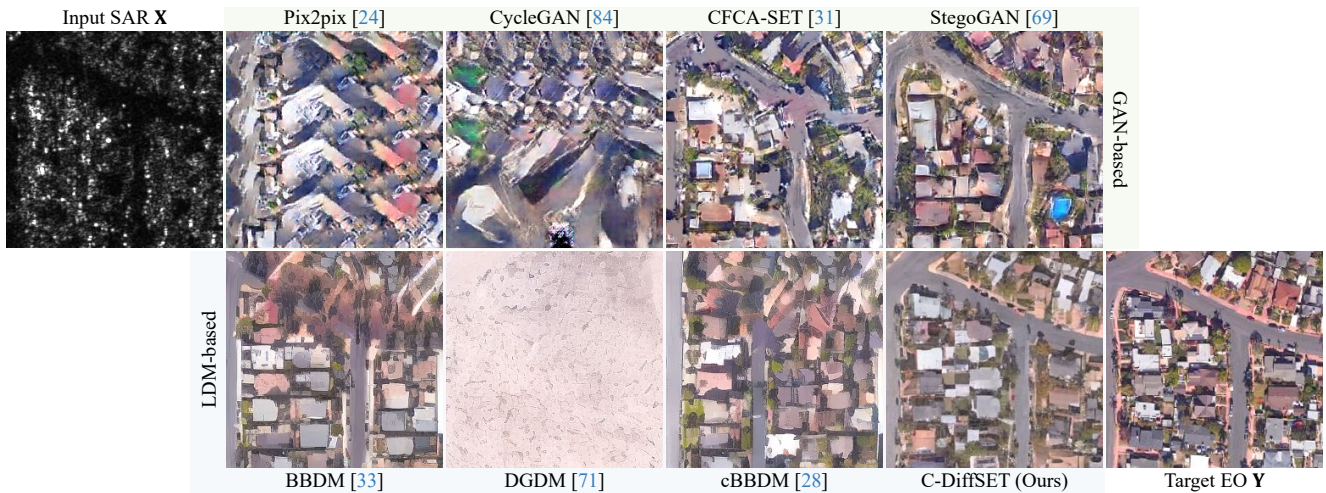


Figure 12. Qualitative SAR-to-EO image translation on the QXS-SAROPT dataset. Top row: GAN-based methods (Pix2pix, CycleGAN, CFCA-SET, and StegoGAN). Bottom row: LDM-based methods (BBDM, DGDM, cBBDM, and C-DiffSET).

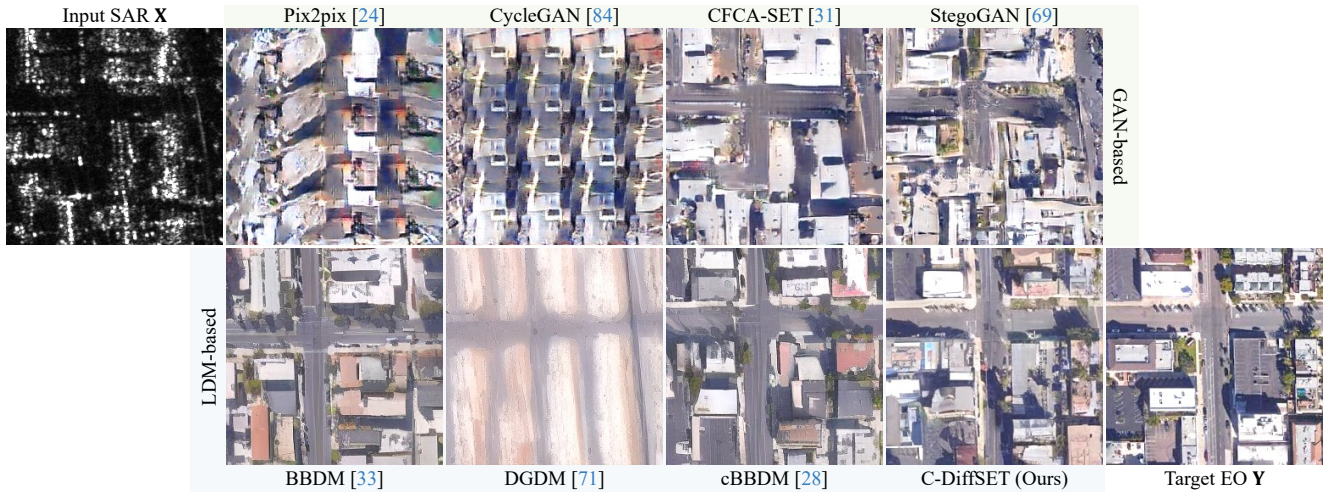


Figure 13. Qualitative SAR-to-EO image translation on the QXS-SAROPT dataset. Top row: GAN-based methods (Pix2pix, CycleGAN, CFCA-SET, and StegoGAN). Bottom row: LDM-based methods (BBDM, DGDM, cBBDM, and C-DiffSET).

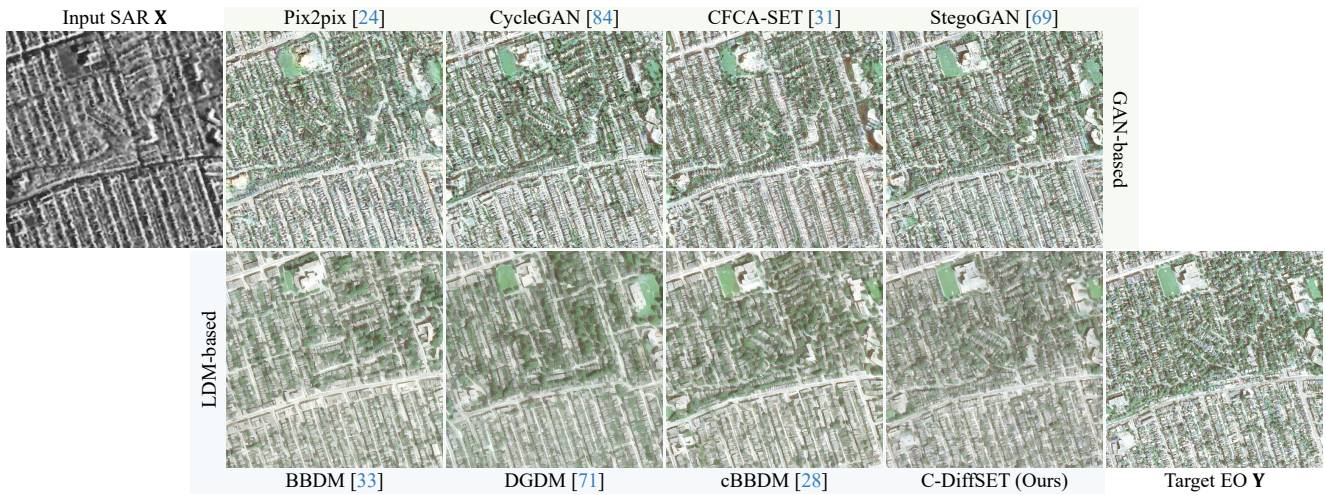


Figure 14. Qualitative SAR-to-EO image translation on the SAR2Opt dataset. Top row: GAN-based methods (Pix2pix, CycleGAN, CFCA-SET, and StegoGAN). Bottom row: LDM-based methods (BBDM, DGDM, cBBDM, and C-DiffSET).

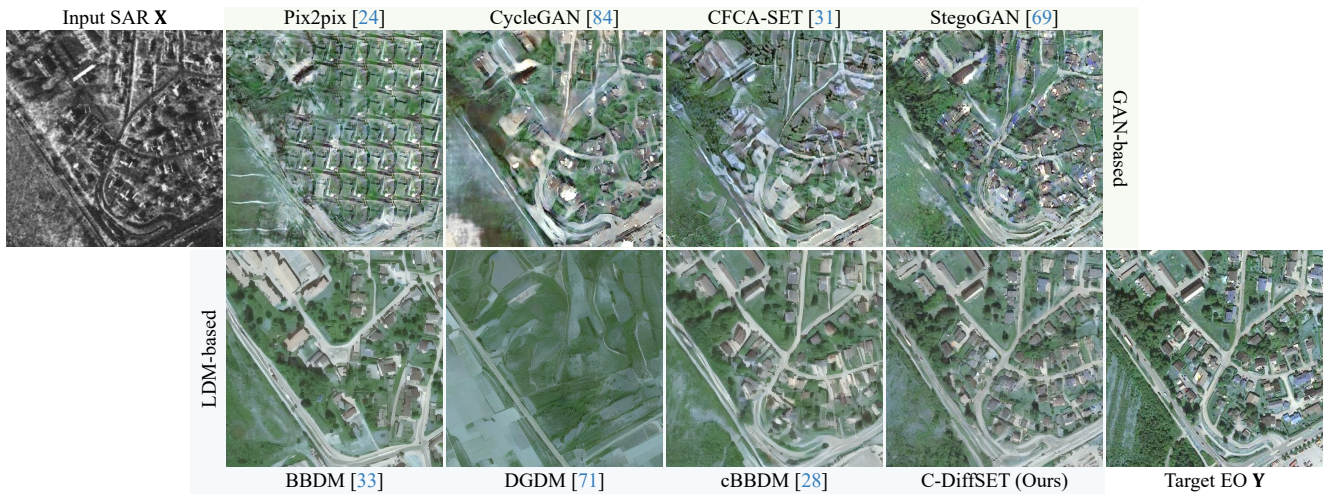


Figure 15. Qualitative SAR-to-EO image translation on the SAR2Opt dataset. Top row: GAN-based methods (Pix2pix, CycleGAN, CFCA-SET, and StegoGAN). Bottom row: LDM-based methods (BBDM, DGDM, cBBDM, and C-DiffSET).

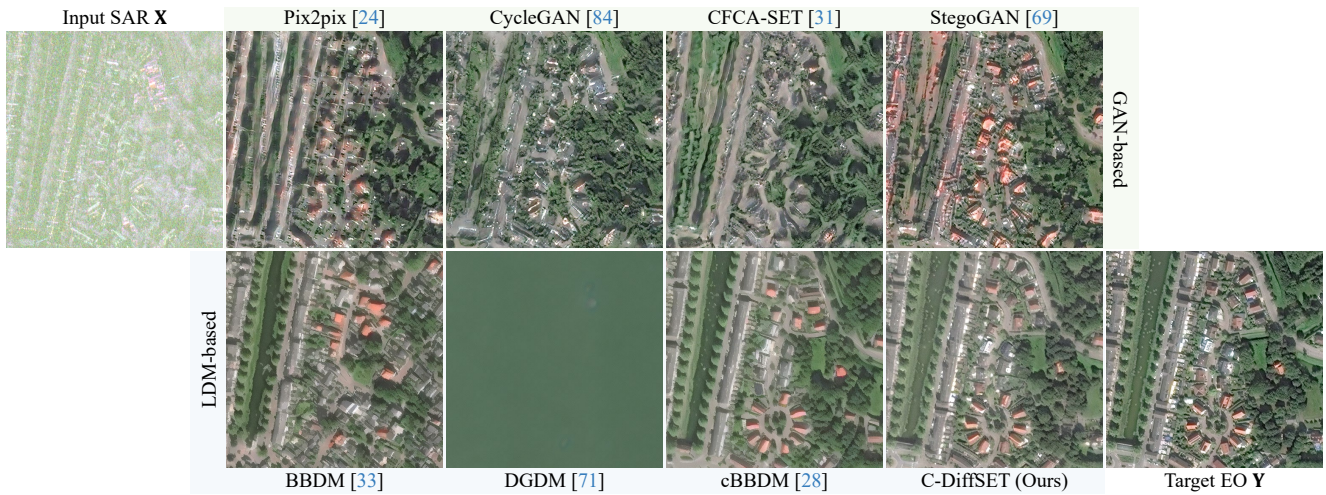


Figure 16. Qualitative SAR-to-EO image translation on the SpaceNet6 dataset. Top row: GAN-based methods (Pix2pix, CycleGAN, CFCA-SET, and StegoGAN). Bottom row: LDM-based methods (BBDM, DGDM, cBBDM, and C-DiffSET).

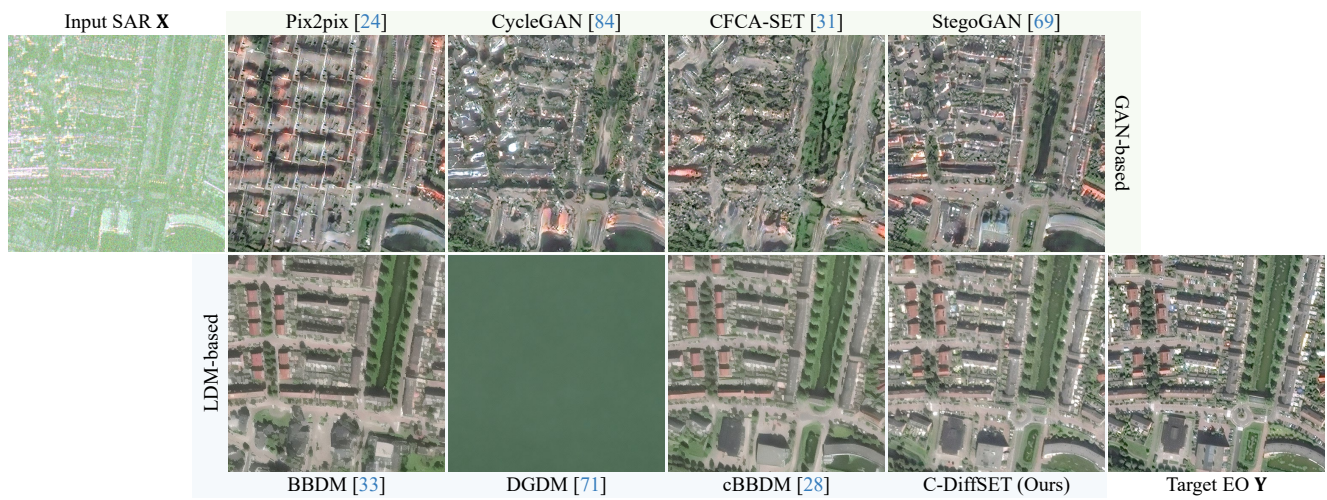


Figure 17. Qualitative SAR-to-EO image translation on the SpaceNet6 dataset. Top row: GAN-based methods (Pix2pix, CycleGAN, CFCA-SET, and StegoGAN). Bottom row: LDM-based methods (BBDM, DGDM, cBBDM, and C-DiffSET).

References

- [1] Kyungjune Baek, Yunjey Choi, Youngjung Uh, Jaejun Yoo, and Hyunjung Shim. Rethinking the truly unsupervised image-to-image translation. In *Proceedings of the IEEE/CVF international conference on computer vision*, pages 14154–14163, 2021. 3
- [2] Xinyu Bai and Feng Xu. Sar to optical image translation with color supervised diffusion model. In *IGARSS 2024-2024 IEEE International Geoscience and Remote Sensing Symposium*, pages 963–966. IEEE, 2024. 3
- [3] Xinyu Bai, Xinyang Pu, and Feng Xu. Conditional diffusion for sar to optical image translation. *IEEE Geoscience and Remote Sensing Letters*, 2023. 3
- [4] Brian Brisco, Masoud Mahdianpari, and Fariba Mohamadimanesh. Hybrid compact polarimetric sar for environmental monitoring with the radarsat constellation mission. *Remote Sensing*, 12(20):3283, 2020. 2
- [5] Armando Cabrera, Miriam Cha, Prafull Sharma, and Michael Newey. Sar-to-eo image translation with multi-conditional adversarial networks. In *2021 55th Asilomar Conference on Signals, Systems, and Computers*, pages 1710–1714. IEEE, 2021. 3
- [6] Runfa Chen, Wenbing Huang, Binghui Huang, Fuchun Sun, and Bin Fang. Reusing discriminators for encoding: Towards unsupervised image-to-image translation. In *Proceedings of the IEEE/CVF conference on computer vision and pattern recognition*, pages 8168–8177, 2020. 3
- [7] Yunjey Choi, Minje Choi, Muniyoung Kim, Jung-Woo Ha, Sunghun Kim, and Jaegul Choo. Stargan: Unified generative adversarial networks for multi-domain image-to-image translation. In *Proceedings of the IEEE conference on computer vision and pattern recognition*, pages 8789–8797, 2018. 3
- [8] Mihai Datcu, Zhongling Huang, Andrei Anghel, Juanping Zhao, and Remus Cacoveanu. Explainable, physics-aware, trustworthy artificial intelligence: A paradigm shift for synthetic aperture radar. *IEEE Geoscience and Remote Sensing Magazine*, 11(1):8–25, 2023. 2, 3
- [9] Kento Doi, Ken Sakurada, Masaki Onishi, and Akira Iwasaki. Gan-based sar-to-optical image translation with region information. In *IGARSS 2020-2020 IEEE International Geoscience and Remote Sensing Symposium*, pages 2069–2072. IEEE, 2020. 3
- [10] Charles Dugas, Yoshua Bengio, François Bélisle, Claude Nadeau, and René Garcia. Incorporating second-order functional knowledge for better option pricing. *Advances in neural information processing systems*, 13, 2000. 5
- [11] Patrick Esser, Sumith Kulal, Andreas Blattmann, Rahim Entezari, Jonas Müller, Harry Saini, Yam Levi, Dominik Lorenz, Axel Sauer, Frederic Boesel, et al. Scaling rectified flow transformers for high-resolution image synthesis. In *Forty-first International Conference on Machine Learning*, 2024. 2, 3, 4
- [12] Jianhao Gao, Qiangqiang Yuan, Jie Li, Hai Zhang, and Xin Su. Cloud removal with fusion of high resolution optical and sar images using generative adversarial networks. *Remote Sensing*, 12(1):191, 2020. 2
- [13] Joseph W Goodman. Some fundamental properties of speckle. *JOSA*, 66(11):1145–1150, 1976. 2, 3
- [14] Zhe Guo, Jiayi Liu, Qinglin Cai, Zhibo Zhang, and Shaohui Mei. Learning sar-to-optical image translation via diffusion models with color memory. *IEEE Journal of Selected Topics in Applied Earth Observations and Remote Sensing*, 2024. 2, 3
- [15] Jing He, Haodong Li, Wei Yin, Yixun Liang, Leheng Li, Kaiqiang Zhou, Hongbo Liu, Bingbing Liu, and Ying-Cong Chen. Lotus: Diffusion-based visual foundation model for high-quality dense prediction. *arXiv preprint arXiv:2409.18124*, 2024. 4
- [16] Martin Heusel, Hubert Ramsauer, Thomas Unterthiner, Bernhard Nessler, and Sepp Hochreiter. Gans trained by a two time-scale update rule converge to a local nash equilibrium. *Advances in neural information processing systems*, 30, 2017. 6
- [17] Jonathan Ho and Tim Salimans. Classifier-free diffusion guidance. *arXiv preprint arXiv:2207.12598*, 2022. 3
- [18] Jonathan Ho, Ajay Jain, and Pieter Abbeel. Denoising diffusion probabilistic models. *Advances in neural information processing systems*, 33:6840–6851, 2020. 3, 5, 6
- [19] Meiyu Huang, Yao Xu, Lixin Qian, Weili Shi, Yaqin Zhang, Wei Bao, Nan Wang, Xuejiao Liu, and Xueshuang Xiang. The qxs-saropt dataset for deep learning in sar-optical data fusion. *arXiv preprint arXiv:2103.08259*, 2021. 3, 6
- [20] Xun Huang, Ming-Yu Liu, Serge Belongie, and Jan Kautz. Multimodal unsupervised image-to-image translation. In *Proceedings of the European conference on computer vision (ECCV)*, pages 172–189, 2018. 3
- [21] Zhongling Huang, Mihai Datcu, Zongxu Pan, and Bin Lei. A hybrid and explainable deep learning framework for sar images. In *IGARSS 2020-2020 IEEE International Geoscience and Remote Sensing Symposium*, pages 1727–1730. IEEE, 2020. 3
- [22] Satoshi Iizuka, Edgar Simo-Serra, and Hiroshi Ishikawa. Globally and locally consistent image completion. *ACM Transactions on Graphics (ToG)*, 36(4):1–14, 2017. 3
- [23] Gabriel Ilharco, Mitchell Wortsman, Nicholas Carlini, Rohan Taori, Achal Dave, Vaishaal Shankar, Hongseok Namkoong, John Miller, Hannaneh Hajishirzi, Ali Farhadi, and Ludwig Schmidt. Open clip, 2021. 6
- [24] Phillip Isola, Jun-Yan Zhu, Tinghui Zhou, and Alexei A Efros. Image-to-image translation with conditional adversarial networks. In *Proceedings of the IEEE conference on computer vision and pattern recognition*, pages 1125–1134, 2017. 3, 6, 8, 9
- [25] Guang Ji, Zhaohui Wang, Lifan Zhou, Yu Xia, Shan Zhong, and Shengrong Gong. Sar image colorization using multidomain cycle-consistency generative adversarial network. *IEEE Geoscience and Remote Sensing Letters*, 18(2):296–300, 2020. 2, 3
- [26] Bingxin Ke, Anton Obukhov, Shengyu Huang, Nando Metzger, Rodrigo Caye Daudt, and Konrad Schindler. Repurposing diffusion-based image generators for monocular depth estimation. In *Proceedings of the IEEE/CVF Conference on Computer Vision and Pattern Recognition*, pages 9492–9502, 2024. 4

- [27] Soohyun Kim, Jongbeom Baek, Jihye Park, Gyeongnyeon Kim, and Seungryong Kim. Instaformer: Instance-aware image-to-image translation with transformer. In *Proceedings of the IEEE/CVF Conference on Computer Vision and Pattern Recognition*, pages 18321–18331, 2022. 3
- [28] Seon-Hoon Kim and Dae-won Chung. Conditional brownian bridge diffusion model for vhr sar to optical image translation. *arXiv preprint arXiv:2408.07947*, 2024. 2, 3, 6, 8, 9
- [29] Diederik P Kingma. Auto-encoding variational bayes. *arXiv preprint arXiv:1312.6114*, 2013. 2
- [30] Yingying Kong, Siyuan Liu, and Xiangyang Peng. Multi-scale translation method from sar to optical remote sensing images based on conditional generative adversarial network. *International Journal of Remote Sensing*, 43(8):2837–2860, 2022. 3
- [31] Jaehyup Lee, Hyebin Cho, Doochun Seo, Hyun-Ho Kim, Jaehoon Jeong, and Munchurl Kim. Cfca-set: Coarse-to-fine context-aware sar-to-eo translation with auxiliary learning of sar-to-nir translation. *IEEE Transactions on Geoscience and Remote Sensing*, 2023. 2, 3, 6, 8, 9
- [32] Jaehyup Lee, Hyun-Ho Kim, Doochun Seo, and Munchurl Kim. Segmentation-guided context learning using eo object labels for stable sar-to-eo translation. *IEEE Geoscience and Remote Sensing Letters*, 2023. 2, 3
- [33] Bo Li, Kaitao Xue, Bin Liu, and Yu-Kun Lai. Bbdm: Image-to-image translation with brownian bridge diffusion models. In *Proceedings of the IEEE/CVF conference on computer vision and pattern Recognition*, pages 1952–1961, 2023. 3, 6, 8, 9
- [34] Xinghua Li, Zhengshun Du, Yanyuan Huang, and Zhenyu Tan. A deep translation (gan) based change detection network for optical and sar remote sensing images. *ISPRS Journal of Photogrammetry and Remote Sensing*, 179:14–34, 2021. 3
- [35] Yahui Liu, Enver Sangineto, Yajing Chen, Linchao Bao, Haoxian Zhang, Nicu Sebe, Bruno Lepri, Wei Wang, and Marco De Nadai. Smoothing the disentangled latent style space for unsupervised image-to-image translation. In *Proceedings of the IEEE/CVF conference on computer vision and pattern recognition*, pages 10785–10794, 2021. 3
- [36] I Loshchilov. Decoupled weight decay regularization. *arXiv preprint arXiv:1711.05101*, 2017. 6
- [37] Ilya Loshchilov and Frank Hutter. Sgdr: Stochastic gradient descent with warm restarts. *arXiv preprint arXiv:1608.03983*, 2016. 6
- [38] ZhiYong Lv, HaiTao Huang, Xinghua Li, MingHua Zhao, Jón Atli Benediktsson, WeiWei Sun, and Nicola Falco. Land cover change detection with heterogeneous remote sensing images: Review, progress, and perspective. *Proceedings of the IEEE*, 110(12):1976–1991, 2022. 2
- [39] Zhiyong Lv, Haitao Huang, Weiwei Sun, Meng Jia, Jón Atli Benediktsson, and Fengrui Chen. Iterative training sample augmentation for enhancing land cover change detection performance with deep learning neural network. *IEEE Transactions on Neural Networks and Learning Systems*, 2023.
- [40] Zhiyong Lv, Pingdong Zhong, Wei Wang, Zhenzhen You, Jón Atli Benediktsson, and Cheng Shi. Novel piecewise distance based on adaptive region key-points extraction for lced with vhr remote-sensing images. *IEEE Transactions on Geoscience and Remote Sensing*, 61:1–9, 2023. 2
- [41] Andrea Meraner, Patrick Ebel, Xiao Xiang Zhu, and Michael Schmitt. Cloud removal in sentinel-2 imagery using a deep residual neural network and sar-optical data fusion. *ISPRS Journal of Photogrammetry and Remote Sensing*, 166:333–346, 2020. 2
- [42] Adam Paszke, Sam Gross, Soumith Chintala, Gregory Chanan, Edward Yang, Zachary DeVito, Zeming Lin, Alban Desmaison, Luca Antiga, and Adam Lerer. Automatic differentiation in pytorch. 2017. 6
- [43] Deepak Pathak, Philipp Krahenbuhl, Jeff Donahue, Trevor Darrell, and Alexei A Efros. Context encoders: Feature learning by inpainting. In *Proceedings of the IEEE conference on computer vision and pattern recognition*, pages 2536–2544, 2016. 3
- [44] William Peebles and Saining Xie. Scalable diffusion models with transformers. In *Proceedings of the IEEE/CVF International Conference on Computer Vision*, pages 4195–4205, 2023. 3
- [45] Dustin Podell, Zion English, Kyle Lacey, Andreas Blattmann, Tim Dockhorn, Jonas Müller, Joe Penna, and Robin Rombach. Sdxl: Improving latent diffusion models for high-resolution image synthesis. *arXiv preprint arXiv:2307.01952*, 2023. 4
- [46] Alec Radford, Jong Wook Kim, Chris Hallacy, Aditya Ramesh, Gabriel Goh, Sandhini Agarwal, Girish Sastry, Amanda Askell, Pamela Mishkin, Jack Clark, et al. Learning transferable visual models from natural language supervision. In *International conference on machine learning*, pages 8748–8763. PMLR, 2021. 5, 6
- [47] Robin Rombach, Andreas Blattmann, Dominik Lorenz, Patrick Esser, and Björn Ommer. High-resolution image synthesis with latent diffusion models. In *Proceedings of the IEEE/CVF conference on computer vision and pattern recognition*, pages 10684–10695, 2022. 2, 3, 4, 6
- [48] Olaf Ronneberger, Philipp Fischer, and Thomas Brox. U-net: Convolutional networks for biomedical image segmentation. In *Medical image computing and computer-assisted intervention—MICCAI 2015: 18th international conference, Munich, Germany, October 5-9, 2015, proceedings, part III 18*, pages 234–241. Springer, 2015. 2
- [49] Chitwan Saharia, William Chan, Huiwen Chang, Chris Lee, Jonathan Ho, Tim Salimans, David Fleet, and Mohammad Norouzi. Palette: Image-to-image diffusion models. In *ACM SIGGRAPH 2022 conference proceedings*, pages 1–10, 2022. 3
- [50] Michael Schmitt, Lloyd Haydn Hughes, and Xiao Xiang Zhu. The sen1-2 dataset for deep learning in sar-optical data fusion. *arXiv preprint arXiv:1807.01569*, 2018. 2, 9
- [51] Christoph Schuhmann, Romain Beaumont, Richard Vencu, Cade Gordon, Ross Wightman, Mehdi Cherti, Theo Coombes, Aarush Katta, Clayton Mullis, Mitchell Wortsman, et al. Laion-5b: An open large-scale dataset for training next generation image-text models. *Advances in Neural Information Processing Systems*, 35:25278–25294, 2022. 4
- [52] Alessandro Sebastianelli, Erika Puglisi, Maria Pia Del Rosso, Jamila Mifdal, Artur Nowakowski,

- Pierre Philippe Mathieu, Fiora Pirri, and Silvia Liberata Ullo. Plfm: Pixel-level merging of intermediate feature maps by disentangling and fusing spatial and temporal data for cloud removal. *IEEE Transactions on Geoscience and Remote Sensing*, 60:1–16, 2022. 2, 3
- [53] Maximilian Seitzer, Arash Tavakoli, Dimitrije Antic, and Georg Martius. On the pitfalls of heteroscedastic uncertainty estimation with probabilistic neural networks. *arXiv preprint arXiv:2203.09168*, 2022. 5, 6
- [54] Minseok Seo, Youngtack Oh, Doyi Kim, Dongmin Kang, and Yeji Choi. Improved flood insights: Diffusion-based sar to eo image translation. *arXiv preprint arXiv:2307.07123*, 2023. 2, 3
- [55] Tamar Rott Shaham, Michaël Gharbi, Richard Zhang, Eli Shechtman, and Tomer Michaeli. Spatially-adaptive pixel-wise networks for fast image translation. In *Proceedings of the IEEE/CVF Conference on Computer Vision and Pattern Recognition*, pages 14882–14891, 2021. 3
- [56] Jacob Shermeyer, Daniel Hogan, Jason Brown, Adam Van Etten, Nicholas Weir, Fabio Pacifici, Ronny Hansch, Alexei Bastidas, Scott Soenen, Todd Bacastow, et al. Spacenet 6: Multi-sensor all weather mapping dataset. In *Proceedings of the IEEE/CVF conference on computer vision and pattern recognition workshops*, pages 196–197, 2020. 3, 6, 9
- [57] Uwe Soergel, Antje Thiele, Hermann Gross, and Ulrich Thoennessen. Extraction of bridge features from high-resolution insar data and optical images. In *2007 Urban Remote Sensing Joint Event*, pages 1–6. IEEE, 2007. 2, 3
- [58] Jiaming Song, Chenlin Meng, and Stefano Ermon. Denoising diffusion implicit models. *arXiv preprint arXiv:2010.02502*, 2020. 6, 9
- [59] Marc Spigai, Céline Tison, and Jean-Claude Souyris. Time-frequency analysis in high-resolution sar imagery. *IEEE Transactions on Geoscience and Remote Sensing*, 49(7):2699–2711, 2011. 3
- [60] Fabio Tosti, Valerio Gagliardi, Fabrizio D’Amico, and Amir M Alani. Transport infrastructure monitoring by data fusion of gpr and sar imagery information. *Transportation Research Procedia*, 45:771–778, 2020. 2
- [61] Thierry Toutin. Three-dimensional topographic mapping with aster stereo data in rugged topography. *IEEE Transactions on geoscience and remote sensing*, 40(10):2241–2247, 2002. 3, 6
- [62] Patrick von Platen, Suraj Patil, Anton Lozhkov, Pedro Cuenca, Nathan Lambert, Kashif Rasul, Mishig Davaadorj, Dhruv Nair, Sayak Paul, William Berman, Yiyi Xu, Steven Liu, and Thomas Wolf. Diffusers: State-of-the-art diffusion models. <https://github.com/huggingface/diffusers>, 2022. 4, 6
- [63] Puyang Wang and Vishal M Patel. Generating high quality visible images from sar images using cnns. In *2018 IEEE Radar Conference (RadarConf18)*, pages 0570–0575. IEEE, 2018. 3
- [64] Yihan Wang, Lahav Lipson, and Jia Deng. Sea-raft: Simple, efficient, accurate raft for optical flow. In *European Conference on Computer Vision*, pages 36–54. Springer, 2025. 5
- [65] Zhou Wang, Alan C Bovik, Hamid R Sheikh, and Eero P Simoncelli. Image quality assessment: from error visibility to structural similarity. *IEEE transactions on image processing*, 13(4):600–612, 2004. 6
- [66] Juan Wei, Huanxin Zou, Li Sun, Xu Cao, Shitian He, Shuo Liu, and Yuqing Zhang. Cfrwd-gan for sar-to-optical image translation. *Remote Sensing*, 15(10):2547, 2023. 3
- [67] Lori White, Brian Brisco, Mohammed Dabboor, Andreas Schmitt, and Andrew Pratt. A collection of sar methodologies for monitoring wetlands. *Remote sensing*, 7(6):7615–7645, 2015. 2
- [68] Rongyuan Wu, Tao Yang, Lingchen Sun, Zhengqiang Zhang, Shuai Li, and Lei Zhang. Seesr: Towards semantics-aware real-world image super-resolution. In *Proceedings of the IEEE/CVF conference on computer vision and pattern recognition*, pages 25456–25467, 2024. 4
- [69] Sidi Wu, Yizi Chen, Samuel Mermet, Lorenz Hurni, Konrad Schindler, Nicolas Gonthier, and Loic Landrieu. Stegogan: Leveraging steganography for non-bijective image-to-image translation. In *Proceedings of the IEEE/CVF Conference on Computer Vision and Pattern Recognition*, pages 7922–7931, 2024. 3, 6, 8, 9
- [70] Yoshio Yamaguchi. Disaster monitoring by fully polarimetric sar data acquired with alos-palsar. *Proceedings of the IEEE*, 100(10):2851–2860, 2012. 2
- [71] Donggeun Yoon, Minseok Seo, Doyi Kim, Yeji Choi, and Donghyeon Cho. Deterministic guidance diffusion model for probabilistic weather forecasting. *arXiv preprint arXiv:2312.02819*, 2023. 3, 6, 8, 9
- [72] Geunhyuk Youk and Munchurl Kim. Transformer-based synthetic-to-measured sar image translation via learning of representational features. *IEEE Transactions on Geoscience and Remote Sensing*, 61:1–18, 2023. 3
- [73] Nir Zabari, Aharon Azulay, Alexey Gorkor, Tavi Halperin, and Ohad Fried. Diffusing colors: Image colorization with text guided diffusion. In *SIGGRAPH Asia 2023 Conference Papers*, pages 1–11, 2023. 4
- [74] Jinsong Zhang, Mengdao Xing, and Yiyuan Xie. Fec: A feature fusion framework for sar target recognition based on electromagnetic scattering features and deep cnn features. *IEEE Transactions on Geoscience and Remote Sensing*, 59(3):2174–2187, 2020. 3
- [75] Jiexin Zhang, Jianjiang Zhou, and Xiwen Lu. Feature-guided sar-to-optical image translation. *Ieee Access*, 8:70925–70937, 2020. 2, 3
- [76] Richard Zhang, Phillip Isola, and Alexei A Efros. Colorful image colorization. In *Computer Vision—ECCV 2016: 14th European Conference, Amsterdam, The Netherlands, October 11–14, 2016, Proceedings, Part III 14*, pages 649–666. Springer, 2016. 3
- [77] Richard Zhang, Jun-Yan Zhu, Phillip Isola, Xinyang Geng, Angela S Lin, Tianhe Yu, and Alexei A Efros. Real-time user-guided image colorization with learned deep priors. *arXiv preprint arXiv:1705.02999*, 2017. 3
- [78] Richard Zhang, Phillip Isola, Alexei A Efros, Eli Shechtman, and Oliver Wang. The unreasonable effectiveness of deep features as a perceptual metric. In *Proceedings of the*

- IEEE conference on computer vision and pattern recognition*, pages 586–595, 2018. 6
- [79] Yueting Zhang, Chibiao Ding, Xiaolan Qiu, and Fangfang Li. The characteristics of the multipath scattering and the application for geometry extraction in high-resolution sar images. *IEEE Transactions on Geoscience and Remote Sensing*, 53(8):4687–4699, 2015. 2, 3
- [80] Yitao Zhao, Turgay Celik, Nanqing Liu, and Heng-Chao Li. A comparative analysis of gan-based methods for sar-to-optical image translation. *IEEE Geoscience and Remote Sensing Letters*, 19:1–5, 2022. 3, 6, 9
- [81] Zhi Zhao, Kefeng Ji, Xiangwei Xing, Huanxin Zou, and Shilin Zhou. Ship surveillance by integration of space-borne sar and ais—review of current research. *The Journal of Navigation*, 67(1):177–189, 2014. 2
- [82] Chuanxia Zheng, Tat-Jen Cham, and Jianfei Cai. The spatially-correlative loss for various image translation tasks. In *Proceedings of the IEEE/CVF conference on computer vision and pattern recognition*, pages 16407–16417, 2021. 3
- [83] Jie Zhou, Daniel L Civco, and John A Silander. A wavelet transform method to merge landsat tm and spot panchromatic data. *International journal of remote sensing*, 19(4):743–757, 1998. 6
- [84] Jun-Yan Zhu, Taesung Park, Phillip Isola, and Alexei A Efros. Unpaired image-to-image translation using cycle-consistent adversarial networks. In *Proceedings of the IEEE international conference on computer vision*, pages 2223–2232, 2017. 3, 6, 8, 9